Asian Journal of Chemistry; Vol. 38, No. 3 (2026), 835-842
ASIAN JOURNAL OF CHEMISTRY
https://doi.org/10.14233/ajchem.2026.35259

Multifunctional Sr-doped Co–Mn Spinel Nanochromites for Antimicrobial and DNA Interaction Applications

R. VENKATESH NAYAK and G. VIJAYA CHARAN*

Department of Chemistry, University College of Science, Osmania University, Hyderabad-500007, India

*Corresponding author: E-mail: drvijayacharan@gmail.com

Received: 18 October 2025 *Accepted*: 26 February 2026 *Published online*: 6 March 2026 AJC-22303

A series of $Co_{0.25}Sr_{0.50}Mn_xCr_{2-x}O_4$ nanochromite samples, where *x* ranges from 0.05, 0.15, 0.25, were prepared by the citrate gel-auto combustion technique. The structural, optical and biological activities of the prepared samples were investigated. A single-phase cubic spinel structure was confirmed by XRD with *Fd*3*m* space group. The crystalline size was found to be in the range of 5.80 to 19.86 nm, calculated using Scherrer formula. FESEM images revealed a spherical and agglomerated structure and the presence of Mn, Co, Sr, Cr and O was confirmed by the EDS spectrum. The presence of M–O bond linkage in tetrahedral and octahedral bands was in the FTIR spectrum. The band gap energy of the samples ranged from 1.93 eV and 1.52 eV calculated using Tauc plots. The biological studies were investigated through antibacterial and antifungal activity using the pour plate method. The synthesized nanospinels exhibited significant antifungal activity against *Candida* and *Aspergillus*, with clear zones of inhibition (~12 mm) and low MIC values (as low as 25 µL), demonstrating strong dose-dependent efficacy. Furthermore, the prepared nanochromites exhibited partial ctDNA cleavage and moderate DNA binding affinity (K_b ~10^4 M^{-1}), indicating weak-to-moderate groove/electrostatic interactions. While antibacterial activity was minimal, the materials demonstrated pronounced antifungal efficacy against *Candida* and *Aspergillus*, with ~12 mm inhibition zones and low MIC values (> 25 µL), confirming composition-dependent and dose-responsive antifungal performance.

Keywords: Spinel nanochromites, Structural properties, Optical direct band gap energy, Microbial activity, DNA binding.

INTRODUCTION

The spinel chromites are a main family of transition-metal oxides with the general formula $A^{2+}B_2^{3+}O_4$ and whose physicochemical properties are strongly controlled by the distribution of cations between tetrahedra (A) shells and octahedra (B) [1-3]. Chromium occurs naturally in the form of chromite ($FeO_2Cr_2O_3$), which is usually formed by differentiation during the igneous formation of ultramafic and metamorphic environments and has historically been the starting material of engineered chromites [4-6]. Due to their high thermal and chemical stability, tunable electronic structure and chemical strength, synthetic chromite spinels have remained of interest to applications in catalysis and optoelectronics [7]. Other spinel systems exhibit a highly enriched redox chemistry and tunable changeable valence state, allowing them to be highly electronically coupled and defect mediated transport.

The substitutional doping, either A-site or B-site, is an effective method of regulating lattice strain, oxygen vacancy concentration and cation disorder which can be used to regulate optical absorption, charge-carrier dynamics and surface reactivity [8,9]. In this context, doping with alkaline-earth metals, particularly strontium (Sr^{2+}), has emerged as a promising yet underexplored strategy. The larger ionic radius of Sr^{2+} compared to typical divalent cations induces lattice distortion and defect formation, which significantly influences the physico-chemical and biological properties of the material [10,11]. In addition to environmental catalysis, recent developments have found that transition metal-based spinel nanomaterials can have large biological activity. The formation of redox-active metal centers, surface charge and production of reactive oxygen species makes the wide-spectrum antimicrobial activity against bacterial and fungal strains possible. Also, metal oxides with nano sizes have been found to react with biomacromolecules, especially, DNA, by utilizing electrostatic attraction, groove binding, intercalation and oxidative cleavage processes [12-14]. This type of DNA binding and

cleavage is of great interest in antimicrobial action, anti-cancer intervention and bio-nano interface engineering.

Though, non-many systematic studies have introduced optical properties with antimicrobial properties and DNA interactions in a single chromite spinel structure. The several traditional synthetic metthods of preparing chromite spinels, including solid-state reaction, hydrothermal processing and mechanical milling, can be characterised by the need of high temperatures, long reaction periods and complicated processing conditions [15,16]. Citrate gel auto-combustion in contrast, is a cost-effective, energy-efficient and environmentally benign process to obtain, in phase-pure form, nanocrystalline spinels with a controlled stoichiometry and homogeneous cation distribution [17,18]. This approach is particularly suitable for defect-engineered and doped spinel systems. In this context, the present work focuses on the synthesis of strontium-doped Co-Mn spinel nanochromites *via* the citrate gel auto-combustion method, followed by a comprehensive investigation of their structural, optical, biological and DNA cleavage and binding properties.

The present work reports the low-temperature synthesis of nanosised samples, $Co_{0.25}Sr_{0.50}Mn_xCr_{2-x}O_4$ samples where *x* ranges from 0.05, 0.15, 0.25 spinel with a confirmed single-phase cubic structure. The multi-cation substitution enabled tunable band gap in the visible region along with ultra-small crystallite size. A comprehensive correlation between structural, optical and biological properties was established. Remarkably, this study reveals broad-spectrum antimicrobial activity and significant DNA interaction behaviour, aspects that are rarely explored in this spinel system. By systematically evaluating antibacterial, antifungal and DNA binding/cleavage properties, the work bridges the gap between conventional chromite-based applications and emerging bio-nanotechnological uses.

EXPERIMENTAL

In the present study, the starting compounds used consist of cobalt nitrate hexahydrate [$Co(NO_3)_2·6H_2O$], strontium nitrate hexahydrate [$Sr(NO_3)_2·6H_2O$], manganese(II) nitrate tetrahydrate [$Mn(NO_3)_2·4H_2O$], chromium nitrate nonahydrate [$Cr(NO_3)_3·9H_2O$], citric acid monohydrate and aqueous ammonia solutions. All chemicals were of analytical reagents (AR) grades, obtained from SD Fine Compounds and were utilised without any further purification.

Synthesis of nanostructured $Co_{0.25}Sr_{0.50}Mn_xCr_{2-x}O_4$ samples: The nanostructured $Co_{0.25}Sr_{0.50}Mn_xCr_{2-x}O_4$ (where x = 0.05, 0.15, 0.25) samples were synthesised using the citrate sol-gel method. In this method, citric acid served both as a chelating agent and as a fuel for the auto-combustions process. According to the required stoichiometric ratios, the synthesis began by dissolving the metal nitrates in distilled water. Th citric acid was then added in a 1:3 molar ratio (nitrates:citric acid) to ensure proper chelation and gel formation. The solution was stirred continuously, and aqueous NH_3 was added dropwise to adjust the pH to neutral (pH ≈ 7). After 2 h of constant stirring to ensure homogeneity, the resultant solutions were heated to 80 ºC. For around 12 h, the reaction mixture was kept untouched. The solution was then allowed to evaporate slowly until its volume reduced to about one-fourth of the original, resulting in the formation of a viscous gel. The temperature was then increased to around 200 ºC to initiate a self-propagating combustion reaction. After ignition, a black fluffy powder was obtained, indicating successful synthesis. The as-formed powder was ground and calcined at 500 ºC for 4 h to improve crystallinity. After cooling, the product was further milled for 1 h to ensure uniform particle size. The resulting nanostructured samples were then used for further characterization [19].

Characterisation: The structural properties and phase purity of the samples were analyzed using a Rigaku Miniflex 600 X-ray diffractometer (XRD). Morphology and particle size were examined by field emissions scanning electron microscopy (FESEM), while elemental composition and distribution were determined using energy disperses X-ray spectroscopy (EDAX) with a ZEISS system. Fourier transforms infrared spectroscopy (FTIR) spectra (4000-400 cm^{-1}) were recorded using a Shimadzu FTIR 8400 to confirm the spinel formation. Optical properties were studied using a Shimadzu UV-3600 spectrophotometer in the 200-400 nm range.

DNA cleavage experiment: The nanochromite samples were dissolved in DMSO and added individually to ctDNA solutions. The mixtures were incubated at 37 ºC for 1 h. DNA cleavage was analyzed by agarose gel electrophoresis. A 1% agarose gel was prepared in 1× TAE buffer (pH 8.0) and allowed to solidify. The DNA samples, mixed with bromophenol blue loading dye, were loaded into the wells along with a control DNA sample. Electrophoresis was carried out at 100 V until the dye front reached the end of the gel. The gel was then stained with ethidium bromide (10 μg/mL) for 10-15 min and DNA bands were visualized under a UV transilluminator.

DNA binding experiment: The interaction of the compounds with ctDNA was studied using UV-Vis absorption spectroscopy (Shimadzu UV-Vis 2600). Measurements were performed in TAE buffer (40 mM Tris-acetate, 1 mM EDTA, pH 7.2) at 25 ºC. During absorption titration, the compound concentration was kept constant at 10 μM, while ctDNA concentration was gradually increased in increments of 20 μM to evaluate binding behaviour.

Antibacterial activity: For antibacterial testing, 1% of actively grown bacterial culture was mixed with sterilized molten agar medium and poured into sterile Petri dishes using the pour plate method. *Staphylococcus* and *Bacillus* were used as Gram-positive strains, while *Escherichia coli* and *Klebsiella* were selected as Gram-negative strains. After the agar solidified, sterile wells were made using a well borer, and 100 μL of each test sample was added to the wells. The plates were incubated at 37 ºC for 18-24 h. The antibacterial activity was evaluated by measuring the zones of inhibition around the wells.

Antifungal activity: The antifungal activity was evaluated using the pour plate method against *Candida* and *Aspergillus* species. Yeast extract peptone agar (YEP) and potato dextrose agar (PDA) were prepared and sterilized by autoclaving. To prevent bacterial contamination, streptomycin or chloramphenicol was added before pouring the media into sterile Petri plates. After solidification, 5 mm wells were prepared using a sterile well borer and 100 μL of each test sample was added

to the wells. The plates were incubated at 25 ºC for 96 h. The antifungal activity was determined by measuring the zones of inhibition around the wells.

RESULTS AND DISCUSSION

XRD studies: Fig. 1 shows the X-ray diffraction (XRD) patterns of the synthesised $Co_{0.25}Sr_{0.50}Mn_xCr_{2-x}O_4$ samples (where x = 0.05, 0.15, 0.25). The XRD pattern shows a single phase cubic spinel structure with the *Fd*3*m* space group and the absence of impurity peaks. The XRD pattern shows the diffraction peaks corresponding to $CoSrCr_2O_4$, in agreement with the reference pattern of the undoped material. The peaks were indexed to the crystallographic planes (011), (200), (220), (221), (311), (213) and (402). The average crystallite size was calculated using Scherrer's formula based on the full width at half maximum (FWHM) of the major diffraction peaks [20].

$$D = \frac{0.94\lambda}{\beta \cos\theta} \quad (1)$$

where λ indicates wavelength, β indicates FWHM and Bragg angle is θ. The average crystalline size ranges from 5.80 to 19.86 nm, with the minimum value of 5.80 nm observed for the x = 0.05 composition. The results confirm that the crystallite size increases progressively with increasing manganese content in the $Co_{0.25}Sr_{0.50}Mn_xCr_{2-x}O_4$ samples. Furthermore, the lattice parameters (a) were calculated [21] using eqn. 2:

$$\text{Lattice parameter (a)} = \sqrt{h^2 + k^2 + l^2} \quad (2)$$

whereas d refers interplanar distance and *hkl* represents the miller indices.

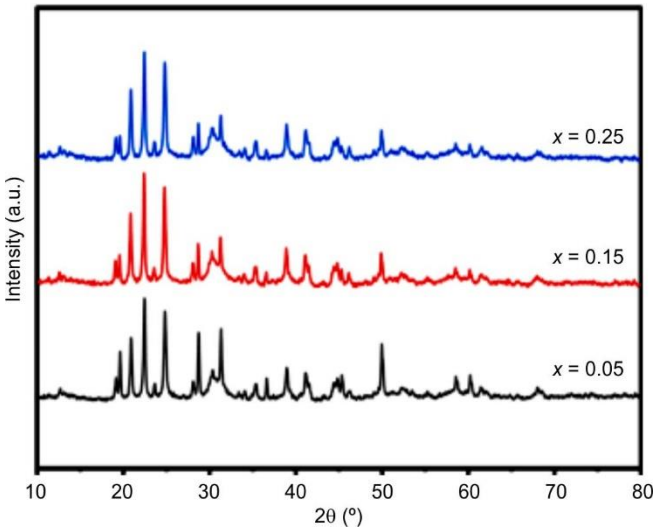

Fig. 1. XRD patterns of $Co_{0.25}Sr_{0.50}Mn_xCr_{2-x}O_4$ (where x = 0.05, 0.15, 0.25)

The lattice parameter varies between 6.434 to 8.452 Å with minimum value found to be 6.434 Å for x = 0.05 composition. Eqn. 3 was used to calculate the unit cell volume of the nanochromite samples.

$$\text{Volume of unit cell (v)} = a^3 \quad (3)$$

where a represents the lattice parameter. The unit cell volume was found be range 553.78-603.88 Å. The crystallite size was initially higher for the x = 0.05 composition, then decreased with further substitution and finally increased up to 603.88 Å. The X-ray density of the samples was calculated using eqn. 3:

$$\text{X-ray density (dx)} = \frac{8M}{Na^3} \quad (4)$$

The X-ray density of the prepared $Co_{0.25}Sr_{0.50}Mn_xCr_{2-x}O_4$ (where x = 0.05, 0.15, 0.25) nanochromites was observed to range from 5.0 to 5.43 g cm^{-3}. The highest X-ray density was observed for the x = 0.15 composition. All the structural parameters obtained from XRD analysis including crystallite size, lattice parameters, X-ray density, unit cell volume and specific surface area, are summarized in Table-1.

FESEM analysis: The prepared samples were being examined for morphological structure and particle size using FESEM. The surface features were studied by the use of secondary electron images to enlarge on the surface characteristics. Fig. 2 shows the FE-SEM images of synthesised nanochromites. The FESEM images of all compositions show similar morphological features, indicating a consistent synthesis process. The particles are mostly spherical and nanosized, in agreement with the crystallite size obtained from XRD analysis [22]. The uniform shape and distribution confirm the formation of nanostructured materials. Moderate agglomeration is observed, with a similar trend in all compositions.

EDAX: Fig. 3 indicates the EDAX spectrum of synthesised $Co_{0.25}Sr_{0.50}Mn_xCr_{2-x}O_4$ (where x = 0.05,0.15, 0.25) nanochromites. The EDS spectra for x = 0.05, 0.15 and 0.25 clearly display peaks corresponding to Co, Sr, Mn, Cr and O (Fig. 3), confirming their presence in all compositions. The atomic and weight percentages listed in Table-1 closely match the expected stoichiometric values, indicating high purity with no detectable impurities. This agreement between the spectra and the tabulated data confirms the successful synthesis of the spinel nanochromites.

FTIR studies: As shown in Fig. 4, the FTIR spectra of $Co_{0.25}Sr_{0.50}Mn_xCr_{2-x}O_4$ (where x = 0.05, 0.15, 0.25) nanochromites shown in Fig. 4, display two main absorption bands around 477 and 625 cm^{-1}, which correspond to metal–oxygen (M–O) vibrations at octahedral and tetrahedral sites, respectively [23]. These bands confirm the formation of the spinel structure with cations occupying both sites. A band near 940 cm^{-1} is attributed to O–H bending vibration, while the broad

TABLE-1
CALCULATED VALUES OF PEAK POSITIONS, FWHM, AVERAGE CRYSTAL LINES SIZE, VOLUMES OF UNIT CELL AND X-RAY DENSITY VALUES OF $Co_{0.25}Sr_{0.50}Mn_xCr_{2-x}O_4$ (where x = 0.05, 0.15, 0.25) NANOCHROMITES

Sample	Peak position 2θ (º)	FWHM (β)	Average crystalline size (D, nm)	Lattice parameters (Å)	Volumes of unit cell (Å)	X-ray density (g cm^{-3})
x = 0.05	30.76	0.348	5.80	6.434	599.99	5.02×10^{-24}
x = 0.15	35.93	0.314	19.88	8.211	553.78	5.43×10^{-24}
x = 0.25	39.87	0.300	16.17	8.452	603.88	5.00×10^{-24}

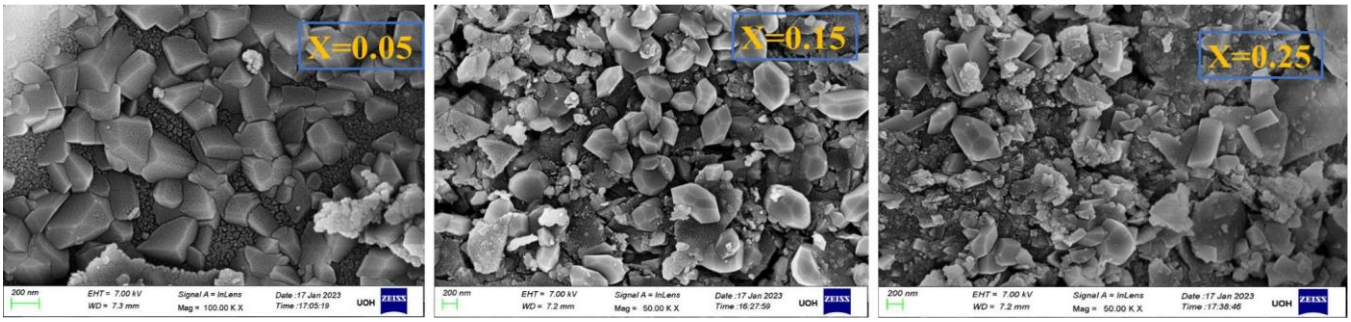

Fig. 2. FESEM micrographs of synthesised $Co_{0.25}Sr_{0.50}Mn_xCr_{2-x}O_4$, x = 0.05,0.15, 0.25.

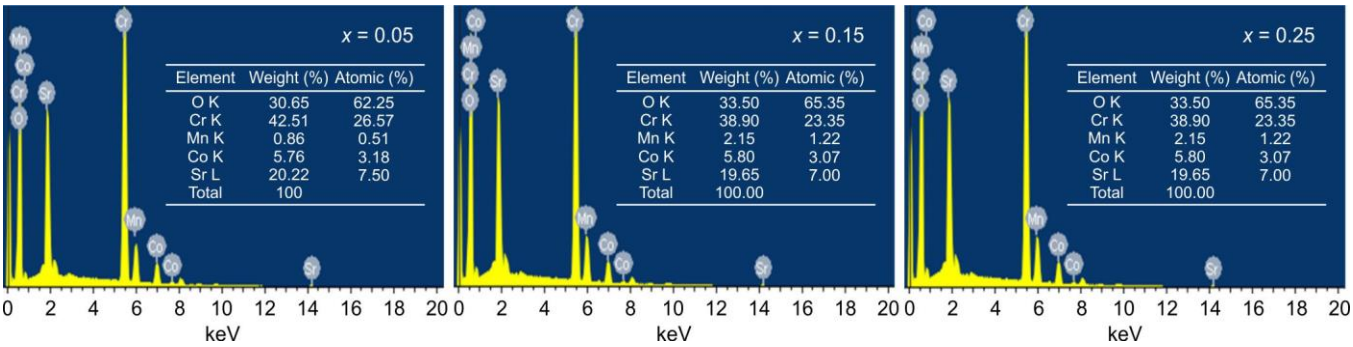

Fig. 3. EDS spectra of $Co_{0.25}Sr_{0.50}Mn_xCr_{2-x}O_4$ (where x = 0.00, 0.05, 0.25)

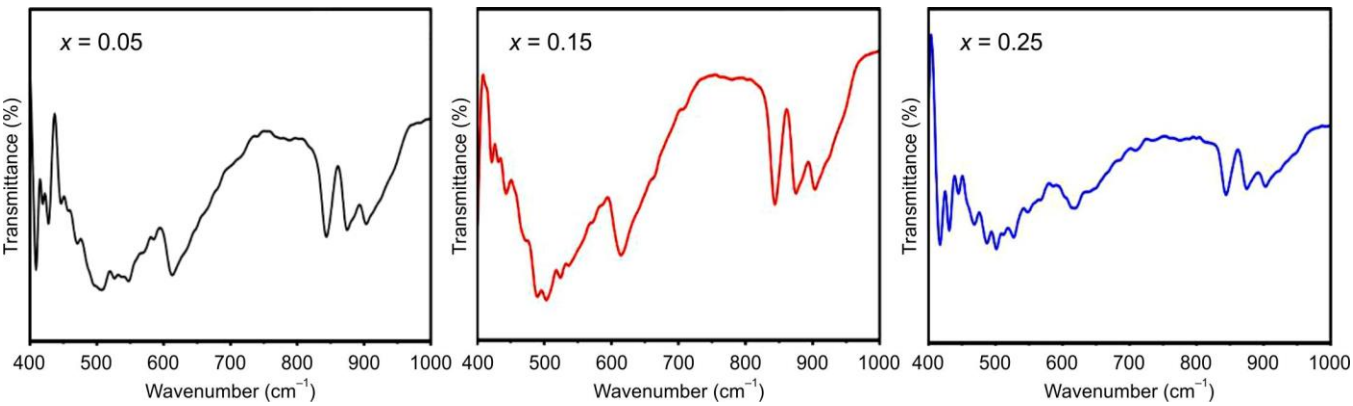

Fig. 4. FTIR spectra of $Co_{0.25}Sr_{0.50}Mn_xCr_{2-x}O_4$ (where x = 0.05, 0.15, 0.25)

band around 3400 cm^{-1} (not shown in this range) is due to O–H stretching, indicating the presence of surface-adsorbed hydroxyl groups.

UV-DRS studies: The UV-DRS spectra (Fig. 5) show strong absorption in the visible region for all compositions, and the absorption intensity increases with increasing Mn content (x = 0.05 to 0.25). A visible red shift in the absorption edge is observed as Mn concentration increases, indicating a reduction in band gap energy. The corresponding Tauc plots (Fig. 6), obtained from the Kubelka-Munk function [$F(R)^2$ *versus* photons energy (hν)], confirm the direct band gap nature of the samples. The extrapolation of the linear region to the energy axis gives band gap values of 1.86 eV (x = 0.05), 1.68 eV (x = 0.15), and 1.52 eV (x = 0.25).

The gradual decrease in band gap with increasing Mn substitution is consistent with the red shift observed in the UV-DRS spectra. This reduction in band gap can be attributed to Mn-induced modification of the electronic structure, possible

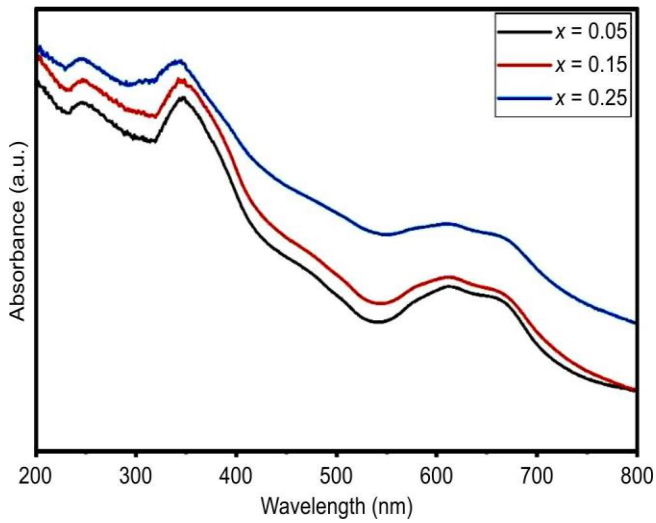

Fig. 5. UV-DRS of $Co_{0.25}Sr_{0.50}Mn_xCr_{2-x}O_4$ (where x = 0.05, 0.15, 0.25)

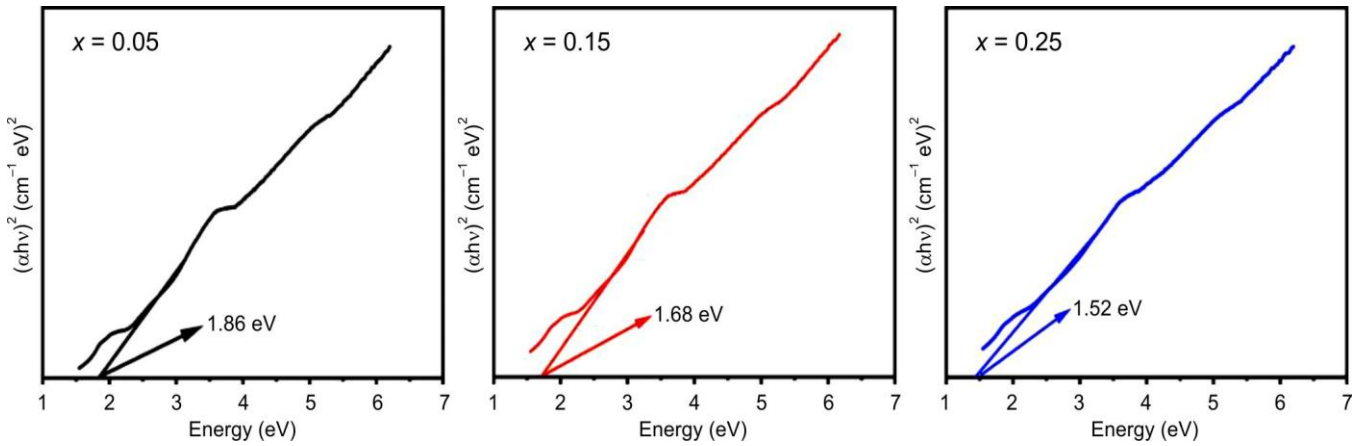

Fig. 6. Tauc plots of $Co_{0.25}Sr_{0.50}Mn_xCr_{2-x}O_4$ (where x = 0.05, 0.15, 0.25)

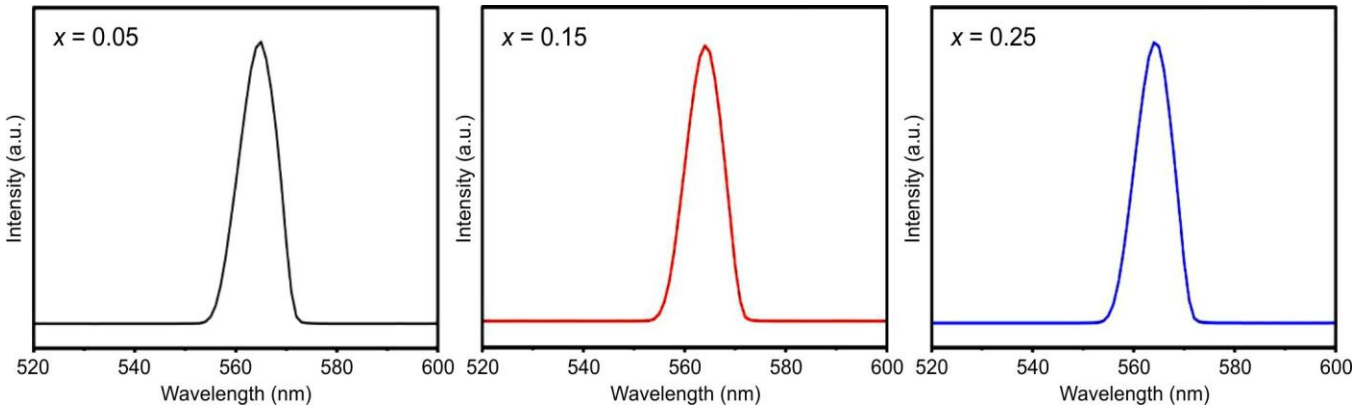

Fig. 7. Fluorescence spectra of $Co_{0.25}Sr_{0.50}Mn_xCr_{2-x}O_4$ (where x = 0.05, 0.15, 0.25)

cation redistribution between tetrahedral and octahedral sites, and the presence of defect states within the spinel lattice [24]. Thus, both UV-DRS and Tauc analysis clearly demonstrate that Mn doping effectively tunes the optical properties of the Co–Mn spinel nanochromites.

Photoluminescence study: As shown in Fig. 7, the PL spectra of $Co_{0.25}Sr_{0.50}Mn_xCr_{2-x}O_4$ (where x = 0.05, 0.15, 0.25), recorded at an excitation wavelength of 300 nm, display a strong emission band in the visible region around 560-580 nm. This emission confirms the radiative recombination of photo-generated electron-hole pairs in the spinel structure. The emission peak position remains nearly the same for all compositions, while the intensity changes with increasing Mn content. This variation in intensity indicates that Mn substitution influences the electronic structure and defect states of the material. The strong visible emission suggests efficient light absorption and recombination processes, which are closely related to the structural characteristics and particle size of the nanochromites [25].

DNA cleavage studies: DNA cleavage was evaluated by agarose gel electrophoresis (Fig. 8). The $Co_{0.25}Sr_{0.50}Mn_xCr_{2-x}O_4$ (where x = 0.05, 0.15, 0.25) nanochromites showed slight DNA cleavage activity. The control sample containing only DNA showed no clear cleavage, confirming that the observed effect is due to the compounds. The gel images indicate partial conversion of supercoiled DNA (Form I) to nicked circular DNA (Form II), suggesting limited strand scission. The extent

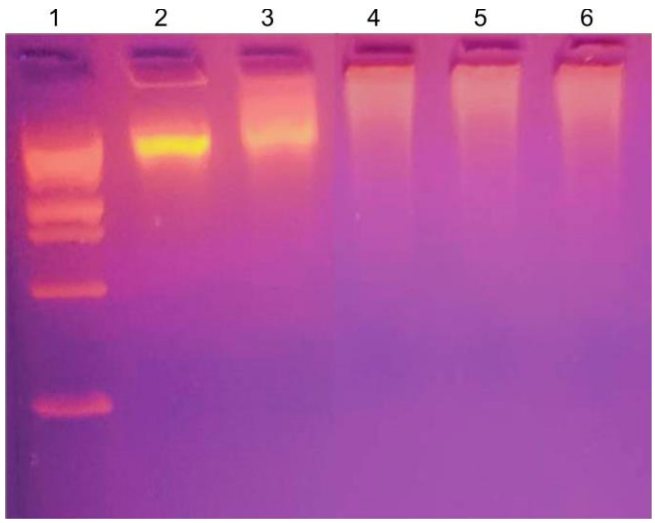

Fig. 8. The cleavage patterns of the compounds observed under trans-illuminator which indicates the presence of components as: Track 1: DNA indicator; Track 2: ctDNA; Track 3: DNA + DMSO; Track 4: 0.05; Track 5: 0.15; Track 6: 0.25

of cleavage varies with Mn content, but the effect remains moderate. Since no mechanistic studies or quantitative band analysis were performed, the cleavage results should be considered preliminary. Further studies, including densitometric analysis and radical scavenger experiments, are required to clarify the cleavage mechanism.

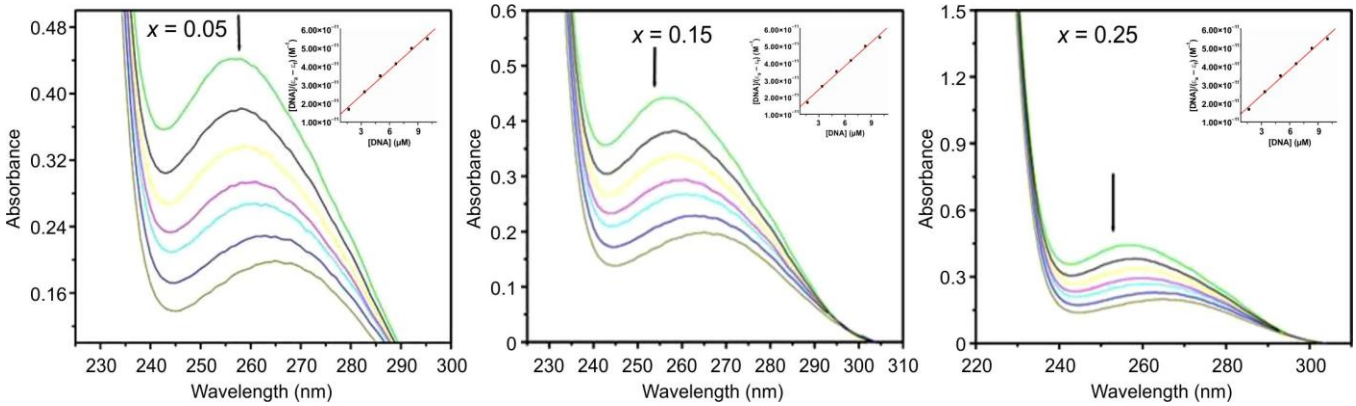

Fig. 9. UV-vis absorption spectra of the complexes showing progressive hypochromic upon ctDNA binding (20, 40, 60 μM); dashed and solid lines represent spectra without and with DNA, respectively. Inset: linear plot used to determine the binding constant (K_b)

DNA binding studies: Upon addition of the compounds to ctDNA, an increase in absorbance intensity along with a slight shift toward longer wavelength (red shift) was observed, indicating interaction between the compounds and DNA. The inset in Fig. 9 shows the linear plot used to calculate the intrinsic binding constant (K_b). The calculated K_b values for x = 0.05, 0.15 and 0.25 are 1.467×10^4, 1.26×10^4 and 1.731×10^4 M^{-1}, respectively. These moderate binding constant values suggest weak to moderate interaction with DNA, likely through groove binding or electrostatic interactions rather than strong intercalation. However, to clearly confirm the exact binding mechanism, further studies such as viscosity measurements, fluorescence displacement assays and reactive oxygen species (ROS) analysis are required.

Antibacterial activity: The antibacterial activity of the synthesised nanochromites was evaluated against Gram-positive (*Staphylococcus*, *Bacillus*) and Gram-negative (*E. coli*, *Klebsiella*) bacteria using the pour plate and well diffusion methods. Table-2 indicates the antibacterial zone of inhibition results of $Co_{0.25}Sr_{0.50}Mn_xCr_{2-x}O_4$ (where x = 0.05, 0.15, 0.25) nanochromites. The zone of inhibition for *Staphylococcus* strains ranged from 4-8 mm, whereas *Bacillus* showed inhibition zones of 4-6 mm. Among these samples, x = 0.05 composition exhibited the highest activity (8 mm) against *Staphylococcus*. In contrast, the samples demonstrated stronger antibacterial activity against Gram-negative bacteria. The zone of inhibition against *E. coli* ranged from 6-12 mm, with x = 0.25 composition showing the highest activity (12 mm). Similarly, significant inhibition was observed against *Klebsiella*, with maximum zones of 8 mm recorded for all samples. All the prepared nanochromite samples exhibited enhanced antibacterial efficiency toward Gram-negative bacteria compared to Gram-positive strains.

TABLE-2
ANTIBACTERIAL ZONE OF INHIBITION VALUE OF $Co_{0.25}Sr_{0.50}Mn_xCr_{2-x}O_4$ (where x = 0.05, 0.15, 0.25) NANOCHROMITES

Sample	Zone of inhibition (mm)			
	Gram-positive bacteria		Gram-negative bacteria	
	Staphylococcus	*Bacillus*	*E. coli*	*Klebsiella*
x = 0.05	8	5	8	8
x = 0.15	6	4	8	8
x = 0.25	4	4	12	8

Table-3 shows the MIC results of prepared nanochromites against Gram-positive (*Staphylococcus*, *Bacillus*) and Gram-negative (*E. coli*, *Klebsiella*) bacteria. The antibacterial activity was evaluated at concentrations of 25, 50, 75 and 100 μL. The results clearly indicate concentration-dependent inhibition for all tested organisms. The composition 0.05 sample *Staphylococcus* exhibited an MIC of 25 μL. *Bacillus*, *E. coli*, and *Klebsiella* showed inhibition beginning at 50 μL, with

TABLE-3
MIC RESULTS OF $Co_{0.25}Sr_{0.50}Mn_xCr_{2-x}O_4$ (where x = 0.05, 0.15, 0.25) NANOCHROMITES

Organism	Sample	Concentration (μL)				MIC (μL)
		25	50	75	100	
Staphylococcus	x = 0.05	4 mm	5 mm	5 mm	8 mm	25
Bacillus		–	4 mm	6 mm	10 mm	50
E. coli		–	5 mm	5 mm	6 mm	50
Klebsiella		–	6 mm	6 mm	7 mm	50
Staphylococcus	x = 0.15	–	-	-	9 mm	100
Bacillus		6 mm	6 mm	8 mm	12 mm	25
E. coli		–	5 mm	5 mm	7 mm	50
Klebsiella		–	6 mm	6 mm	8 mm	50
Staphylococcus	x = 0.25	–	-	4 mm	7 mm	75
Bacillus		5 mm	6 mm	6 mm	10 mm	25
E. coli		–	6 mm	8 mm	8 mm	50
Klebsiella		–	5 mm	5 mm	6 mm	50

MIC values of 50 μL. The composition 0.15 sample exhibits higher MIC value (100 μL) against *Staphylococcus*, whereas, *Bacillus* showed a low MIC of 25 μL. *E. coli* and *Klebsiella* both exhibited MIC values of 50 μL. Similarly, the composition 0.25 sample showed an MIC of 75 μL against *Staphylococcus* and 25 μL against *Bacillus*. *E. coli* and *Klebsiella* again exhibited MIC values of 50 μL. The results of MIC data reveal that *Bacillus* was more sensitive to most nanoparticle compositions, showing consistently low MIC values (25 μL). *Staphylococcus* displayed variable sensitivity depending on the composition. Gram-negative bacteria generally required 50 μL for inhibition, except in $x = 0.05$ composition where *E. coli* required 100 μL. These findings confirm that antibacterial efficiency is both concentration- and composition-dependent.

Antifungal activity: The antifungal activity of the prepared nanochromites was also evaluated against *Candida* and *Aspergillus* species using the agar well diffusion method. Tables 4-6 collectively confirm the antifungal effectiveness of prepared nanochromites and show a clear composition- and concentration-dependent behaviour.

TABLE-4
ANTIFUNGAL ACTIVITY ZONE OF INHIBITION OF *Aspergillus* $Co_{0.25}Sr_{0.50}Mn_xCr_{2-x}O_4$ (where x = 0.05, 0.15, 0.25) NANOCHROMITES

Sample	Fungal pathogens	
$x = 0.05$	12 mm	> 20
$x = 0.15$	10 mm	> 20
$x = 0.25$	12 mm	> 20

TABLE-5
MIC VALUES *Candida* OF $Co_{0.25}Sr_{0.50}Mn_xCr_{2-x}O_4$ (where x = 0.05, 0.15, 0.25) NANOCHROMITES

Sample	Concentration (μL)				MIC (μL)
	25	50	75	100	
$x = 0.05$	–	6	6	10	50
$x = 0.15$	–	–	6	8	75
$x = 0.25$	–	6	8	10	75

TABLE-6
MIC VALUES *Aspergillus* OF $Co_{0.25}Sr_{0.50}Mn_xCr_{2-x}O_4$ (where x = 0.05, 0.15, 0.25) NANOCHROMITES

Sample	Concentration (μL)				MIC (μL)
	25	50	75	100	
$x = 0.05$	16	16	16	>20	25
$x = 0.15$	6	16	16	>20	25
$x = 0.25$	6	6	16	16	25

Table-4 shows that most compositions exhibit good antifungal activity with zones of inhibition of about 12 mm, except the $x = 0.15$ composition sample, which shows relatively lower activity. Table-5 indicates that against *Candida*, the lowest MIC value (50 μL) was observed for $x = 0.15$ and $x = 0.25$ composition samples, while other composition required higher concentrations (75 μL), reflecting moderate variation in potency with Mn content. Table-6 further demonstrates that all compositions show strong activity against *Aspergillus*, with low MIC values of 25 μL, confirming effective antifungal performance at low concentrations. Thus, these dilutions were prepared by mixing the stock solution with solvent in defined ratios [26]. The results confirm that antifungal activity varies with concentration, providing insight into the dose-dependent efficacy of the Co-Sr-Mn nanochromite compounds [27].

Conclusion

The nanochromites, $Co_{0.25}Sr_{0.50}Mn_xCr_{2-x}O_4$ (where x = 0.05, 0.15, 0.25), were successfully prepared by the citrate gel-auto combustion technique. Citric acid was used as both a chelating agent and fuel. The average crystalline size ranges from 5.80 to 19.86 nm, with the minimum value of 5.80 nm observed for the $x = 0.05$ composition. The XRD of the nanochromites was found to range from 5.0 to 5.43 g cm^{-3}. FESEM analysis revealed predominantly spherical nanoparticles in the nanoscale range, consistent with the crystallite sizes estimated from XRD. FTIR spectra displayed characteristic bands at 477, 625 and 940 cm^{-1}, corresponding to metal–oxygen vibrations (Co–O, Mn–O and Cr–O), confirming the formation of the spinel framework. The optical band gap decreased systematically from 1.93 eV to 1.52 eV with increasing Mn substitution, indicating modification of the electronic structure due to the cation substitution and possible defect states within the lattice. The biological evaluation showed significant antifungal activity against *Candida* and *Aspergillus*, with inhibition zones of approximately 12 mm for most compositions. These results demonstrate that the prepared nanochromites possess tunable structural and optical properties along with promising antimicrobial potential.

ACKNOWLEDGEMENTS

The authors are thankful to the Head, Department of chemistry, Osmania University, Hyderabad for the providing the research facilities.

CONFLICT OF INTEREST

The authors declare that there is no conflict of interests regarding the publication of this article.

DECLARATION OF AI-ASSISTED TECHNOLOGIES

During the preparation of this manuscript, the authors used an AI-assisted tool(s) to improve the language. The authors reviewed and edited the content and take full responsibility for the published work.

REFERENCES

1. I. El Hajjar, M.A. Bitar, R. Zahr, S. Zahr, M. Khalil and R. Awad, *Mater. Res. Express*, **11**, 015003 (2024); https://doi.org/10.1088/2053-1591/ad1774
2. N. Lotfian, A.A. Nourbakhsh, S.N. Mirsattari, A. Saberi and K.J.D. Mackenzie, *Ceram. Int.*, **46**, 747 (2020); https://doi.org/10.1016/j.ceramint.2019.09.028
3. Y. El Jabbar, H. Lakhlifi, R. El Ouatib, L. Er-Rakho, S. Guillemet-Fritsch and B. Durand, *Ceram. Int.*, **47**, 9373 (2021); https://doi.org/10.1016/j.ceramint.2020.12.068
4. T. Garg, A.A. Koser and A. Yadav, *Next Research*, **2**, 100599 (2025); https://doi.org/10.1016/j.nexres.2025.100599
5. K. Vanasundari, G. Mahalakshmi and A. Prakasam, *Next Materials*, **4**, 100196 (2024); https://doi.org/10.1016/j.nxmate.2024.100196

6. F. Muhammad, M. Xia, S. Li, X. Yu, Y. Mao, F. Muhammad, X. Huang, B. Jiao, L. Yu and D. Li, *J. Clean. Prod.*, **234**, 381 (2019); https://doi.org/10.1016/j.jclepro.2019.06.004
7. D. Harrabi, S. Hcini, I. Ghiloufi, A. Mimouni, J. Dhahri and K. Khirouni, *J. Magn. Magn. Mater.*, **582**, 171040 (2023); https://doi.org/10.1016/j.jmmm.2023.171040
8. S. Heni, S. Hcini, M.L. Bouazizi, L. HajTaieb, A. Dhahri and H. Bacha, *RSC Advances*, **14**, 26340 (2024); https://doi.org/10.1039/D4RA03342F
9. R. Michalsky, B.A. Peterson and P.H. Pfromm, *Thermochim. Acta*, **582**, 10 (2014); https://doi.org/10.1016/j.tca.2014.02.018
10. M. Pazoki, T.J. Jacobsson, A. Hagfeldt, G. Boschloo and T. Edvinsson, *Phys. Rev. B*, **93**, 144105 (2016); https://doi.org/10.1103/PhysRevB.93.144105
11. J. Wang, Y. Wang, M. Zheng and F. Cai, *Materials*, **18**, 1320 (2025); https://doi.org/10.3390/ma18061320
12. J.C.L. Chow, *AIMS Biophys.*, **11**, 340 (2024); https://doi.org/10.3934/biophy.2024019
13. R.K. Shukla, A. Badiye, K. Vajpayee and N. Kapoor, *Front. Genet.*, **12**, 728250 (2021); https://doi.org/10.3389/fgene.2021.728250
14. H. An and B. Jin, *Biotechnol. Adv.*, **30**, 1721 (2012); https://doi.org/10.1016/j.biotechadv.2012.03.007
15. Z. Shao, X. Wu, X. Wu, S. Feng and K. Huang, *Mater. Chem. Front.*, **7**, 5288 (2023); https://doi.org/10.1039/D3QM00416C
16. Q. Zhao, Z. Yan, C. Chen and J. Chen, *Chem. Rev.*, **117**, 10121 (2017); https://doi.org/10.1021/acs.chemrev.7b00051
17. P.S. Kumari, D.R. Kumar and G.V. Charan, *J. Sol-Gel Sci. Technol.*, **113**, 296 (2025); https://doi.org/10.1007/s10971-024-06605-4
18. P.S. Kumari, D.R. Kumar and G.V. Charan, *ChemistrySelect*, **10**, e00600 (2025); https://doi.org/10.1002/slct.202500600
19. D.R. Kumar, C.A. Lincoln, D. Ravinder and S.I. Ahmad, *Appl. Phys., A Mater. Sci. Process.*, **126**, 705 (2020); https://doi.org/10.1007/s00339-020-03894-8
20. A.A.H. El-Bassuony and H.K. Abdelsalam, *J. Mater. Sci. Mater. Electron.*, **31**, 3662 (2020); https://doi.org/10.1007/s10854-020-02924-8
21. Ch. Srikanth, P.S. Kumari, R.V. Nayak and G.V. Charan, *Asian J. Chem.*, **37**, 729 (2025); https://doi.org/10.14233/ajchem.2025.33195
22. P. Gurusamy, A. Gnanasekar and G. Deivasigamani, Investigation of Structural, Morphological, Optical, and Dielectric Properties of Magnesium Chromite (MgCr2O4) Spinel Oxide, in: The 5th International Electronic Conference on Applied Sciences, MDPI, Basel Switzerland, 2025: p. 109; https://doi.org/10.3390/engproc2025087109
23. D. Ravi Kumar, C.A. Lincoln, G. Vijaya Charan, G. Thara, D. Ravinder, M. Veeraswamy and P. Naresh, *Mater. Chem. Phys.*, **278**, 125648 (2022); https://doi.org/10.1016/j.matchemphys.2021.125648
24. P. Sailaja Kumari, G. Vijaya Charan and D. Ravi Kumar, *Inorg. Chem. Commun.*, **139**, 109393 (2022); https://doi.org/10.1016/j.inoche.2022.109393
25. P.S. Kumari, D.R. Kumar, G.V. Charan and S.R. Sagurthi, *Chem. Zvesti*, **77**, 4727 (2023); https://doi.org/10.1007/s11696-023-02798-0
26. M.A. Sayed, T.M.A.A. El-Rahman, H.K. Abdelsalam, A.M. Ali, M.M. Hamdy, Y.A. Badr, N.H.A.E. Rahman, S.M.A. El-Latif, S.H. Mostafa, S.S. Mohamed, Z.M. Ali and A.A.H. El-Bassuony, *BMC Chem.*, **16**, 39 (2022); https://doi.org/10.1186/s13065-022-00832-y
27. C. Srikanth, P. Sailaja Kumari, D. Ravi Kumar, D. Ayodhya and G. Vijaya Charan, *Results in Surfaces and Interfaces*, **20**, 100599 (2025); https://doi.org/10.1016/j.rsurfi.2025.100599